Received: 19 August 2024 | Revised: 7 December 2024 | Accepted: 20 December 2024

DOI: 10.1002/VIW.20240077

VIEW

RESEARCH ARTICLE

Engineering of hierarchical nano-convex polymer lattice SERS platforms by template replica-assisted nanoimprinting

Gohar Ijaz Dar[1] | **Elisabet Xifre-Perez**[1] | **Abel Santos**[2,3] | **Lluis F. Marsal**[1]

[1]Departament d'Enginyeria Electrònica, Elèctrica i Automàtica, Universitat Rovira i Virgili, Tarragona, Spain

[2]School of Chemical Engineering, The University of Adelaide, Adelaide, South Australia, Australia

[3]Institute for Photonics and Advanced Sensing, The University of Adelaide, Adelaide, South Australia, Australia

Correspondence
Lluis F. Marsal, Departament d'Enginyeria Electrònica, Elèctrica i Automàtica, Universitat Rovira i Virgili, Tarragona, Spain.
Email: lluis.marsal@urv.cat

Funding information
European Union's Horizon 2020, Grant/Award Number: 945413; Spanish Ministerio de Ciencia e Innovación (MICINN/FEDER); Agency for Management of University and Research Grants (AGAUR); COST Action 20126-NETPORE, and the Catalan Institution for Research and Advanced Studies (ICREA); Australian Research Council, Grant/Award Number: DP220102857

Abstract

The precise fabrication of arrays of gold and silver nanodots (Au&Ag_NDs) to create plasmonic lattices on different substrates through cost-effective, scalable approaches remains challenging. The aim of this research is to engineer a new class of hierarchical plasmonic lattices based on Au&Ag_NDs generated on polymer substrates via template replica-assisted nanoimprinting. This method harnesses a combination of nanopatterning via anodization, magnetron sputtering, and annealing to generate Au&Ag_NDs hierarchical plasmonic lattices with tunable features at the nanoscale. These plasmonic lattices are explored as ultrasensitive surface-enhanced Raman scattering (SERS) platforms for the detection of a model organic (rhodamine B [RhB]). These reproducible model platforms achieve remarkable enhancement to detect RhB molecules, with a low limit of detection of 10^{-8} M. The enhancement field factor of 10^{7} indicates that the developed plasmonic lattices are adequate for efficient and highly sensitive SERS detection.

KEYWORDS
hierarchical structures, nanodots, nanoimprinting, SERS sensing, plasmonic lattices, optical engineering

1 | INTRODUCTION

To understand the mechanisms that enhance localized electromagnetic fields in surface-enhanced Raman scattering (SERS) platforms is critical for a variety of applications in medical diagnosis, food safety, forensic science, and environmental analyses.[1] At the core of SERS are localized surface plasmon resonances (LSPRs), which are strong localizations of incident electromagnetic waves in nanostructures (e.g., gaps, cracks, and sharp edges) based on noble metals and semiconductors.[2] SERS "hot spots"—highly localized regions of intense local field enhancement caused by the plasmonic coupling of noble metal nanostructures—locally enhance the electromagnetic field by several orders of magnitude (by a factor of ~10^{10}–10^{15}).

Within spaces that are several orders of magnitude smaller than the wavelength of light.[3] SERS hot spots

can be precisely engineered through structural and compositional modifications of metallic nanostructures. Some examples are three-dimensional (3D) SERS platforms based on colloidal nanodots and two-dimensional (SERS) lattices and superlattices combining distinct forms of metal-based nanostructures.[4] Clara and colleagues used these platforms to investigate and track cell behavior in 3D structures, which remains challenging. They proposed a framework for real-time SERS biosensing and bioimaging of breast cancer 3D tumoroids. They promote for the use of multifunctional scaffolds to study intricate cell cultures and demonstrate the adaptability of 3D-printed plasmonic scaffolds for SERS biosensing and bioimaging.[5] In another work, Aziz and coworkers reported the methodology includes drop-casting and thin metal layer deposition to make micromotors, a two-dimensional (2D) COMSOL simulation model to study Au-nanodots' effect on the absorption signal, and Au nanorod and nano star tracking strategies to improve specificity and contrast in imaging.[6] Wang et al. investigated the production of superlattice surface lattice resonances (SLRs) using plasmonic nanoparticle (NPs) lattices featuring dielectric patches, the capacity to sustain quadrupole excitations with unique dispersion diagrams, and the adjustability of optical responses in 2D nanophononics using patterned dielectric patches.[7] Guan et al. described the successful understanding of a plasmonic white-light laser employing a sandwiched lattice structure with combined dye solutions to control relative lasing emission intensities for a wide range of additive colors.[8] Further improvements can be made by integrating plasmonic NP lattices with more efficient gain media. Their research on modulating lasing colors in tiny structures has ramifications for display technology, on-chip optical communications, and light-induced chemical processes. Structurally engineered SERS platforms are particularly interesting for sensing applications and have demonstrated outstanding capabilities for molecular-level detection of analytes. The fundamental idea of this technology is based on the premise that plasmonic nanostructures, composed of metals such as copper, silver, and gold, significantly amplify the Raman signals of analytes after these are absorbed onto the nanostructures' surfaces.[9] SERS can analyze a wide range of analytes with simplicity, rapidly, and ultra-low sensitivity (i.e., single molecule level) using a non-destructive detection approach that generates a unique spectroscopic signature of the analyte of interest for molecular fingerprinting.[10]

Lithography, solvothermal (or hydrothermal) reaction, electrodeposition, galvanic replacement, and reduction assisted by ultrasonication are some of the methods that have been reported for the creation of noble metal-based nanostructures.[11] Gold and silver (Au&Ag) patterned fractals are complex to synthesize on flat or curved surfaces, where they can be employed as a reagent-free, ultrasensitive SERS substrates. The way in which noble metals nanoarrays are structured is strongly dependent on the topography of the template.[12] The spatial resolution of sputtered metallic nano-assemblies is controlled by the template morphology, and it is a critical design factor for plasmonic applications such as surface-enhanced Raman fluorescence and spectroscopy.[13]

The rigid substrate accommodates the bulk of SERS active components. For in situ, real-time SERS detection, it is necessary to use flexible or soft platforms that can be easily attached to uneven surfaces of objects by someone without specialized training. The research and application of flexible SERS platforms—made of materials such as polymer, paper, adhesive tape, cotton, and carbon cloth—has attracted extensive research efforts due to their numerous benefits over rigid SERS platforms. [14–16] These advantages include being more portable, highly flexible, hold great promise for employing in 2D and 3D dimensions flexible sensors—biochemical sensing, implantable devices, wearable electronics, and health monitoring devices.[17,18] Materials made of flexible polymers that are lightweight, translucent, and easy to manufacture are frequently used. Polymethyl methacrylate (PMMA), poly-dimethylsiloxane, and polyvinyl chloride are just a few examples of comparable polymers.[19,20] Analyte molecules on non-flat surfaces can be detected in real-time without damage by covering the sample surface closely. The use of self-assembly and template-assisted technologies are alternatives to fabricate noble metal NP lattices. By linking hybrid plasmonic and photonic resonances through optimized structural designs, 2D nano-plasmonic lattices created by these cost-competitive techniques have been shown to offer enhanced electromagnetic field performances for SERS applications.[21] Despite recent achievements, to control the homogeneity of these structures at the nano- and macroscopic scales to operate at the visible–NIR spectral range remains challenging. An important step towards comprehending and making use of complicated hybrid plasmonic resonance modes for SERS is the development of model metal-based NP lattices integrated into functional platforms with appropriate shapes and features. To enable the bench-to-field transition and keep the costs of technological translation to a minimum, these advancements will necessitate nanofabrication methods that are fully scalable, cost-competitive, and compatible with existing fabrication processes. Electrochemical oxidation of aluminum, also known as anodization, produces self-organized nanoporous anodic alumina (NAA), which provides a unique platform material to develop many photonic and plasmonic structures because of its malleability and well-defined geometric features at the nanoscale.[22] At its base, NAA showcases arrays of self-assembled

hemispherical nanocaps that are hexagonally organized and have an interpore spacing or lattice constant that can be fine-tuned from 60 to 700 nm through the input anodization voltage.[23] In the process of anodization, a mirror image of the hemispherical nanocaps on NAA is transferred to the underlying aluminum substrate through a self-organizing, mechanoelectrochemical growth mechanism. The oxide layer that forms at the interface between the oxide and metal expands in volume (i.e., the Pilling–Bedworth ratio is approximately 1.2342) and patterns the aluminum substrate with arrays of triangular lattices of hemispherical nanoconcavities, created by selectively removal of the NAA layer via wet chemical etching.[24,25] By integrating anodization, metal coating, and thermal sintering, Ikeda and colleagues have proved that it is possible to fabricate highly ordered arrays of Au nanodots on nanopatterned aluminum platforms.[26] Here, we provide a simple, flexible, and inexpensive non-lithographic nanofabrication method for 2D gold and silver nanodot plasmonic single lattices (Au&Ag_ND-PSLs) that have been constructed and designed with exact optical characteristics for visible–NIR light-driven SERS. By changing the anodization voltage from 25 to 195 V, nanopatterned aluminum substrates with hemispherical nanoconcavity arrays in a triangular pattern were created. The geometry of these nanoconcavities ranged from approximately 40 to 512 nm in diameter, and the lattice constant was between 60 and 550 nm. Using nanopatterned aluminum substrates as templates, gold and silver nanodot arrays were created by metal sputtering and thermal sintering. Structural engineering of the Au nanodot arrays controlled the properties of the LSPR bands of Au&Ag_ND-PSLs across the visible spectrum range. Researchers are highly interested in finding ways to apply photoreduced metal nanodots on rigid templates efficiently so that they can meet the desired condition, which involves the efficient mass transfer of noble-metal nanodots from the template to the flexible polymer-based substrate. By selectively dissolving aluminum substrates through chemical etching, functionalized Au&Ag_ND-PSLs nanodot fractals were transferred to PMMA films (Scheme 1). This approach presents numerous benefits compared to earlier methodologies.

2 | RESULTS AND DISCUSSION

2.1 | Structural and optical measurement of PMMA platforms

To acquire the required morphology for SERS activity, we employed various steps initiated from the Al concavities dressed with Au&Ag to transfer to PMMA membrane. The final morphology of platforms was confirmed using the field-emission scanning electron microscope (FESEM) images that reflected its metal composition and nanostructure arrangements. Initially the sputtered Au&Ag metals on concavities and then thermally annealed at various temperatures resultantly revealed the pattern of Au&Ag.

The FESEM images revealed the resultant morphology of the PMMA nanostructure exact replica of the Al nano concavities, as shown in Figure 1. This initial step showed the formation of the nanostructure of PMMA, which potentially gives the direction for next steps to get the decoration of the Au&Ag nanofractals on PMMA hierarchical structures (PMMA-HRs). We proceed our experiments to the next step toward the decoration of Au&Ag nanofractals onto surface of PMMA-HRs. The FESEM image revealed the Au nanofractals trapped onto PMMA surface, as shown in Figure 2. The Au with sputtering of 90 and 120 s after thermally annealed at 400°C for 30 min showed various magnifications. The reduction of surface energy is the main incentive behind the production of NPs, as Willson and others have proved for morphologies that are comparable.[27] However, the Au sputtering and morphology of template determines the resultant size homogeneity and distribution of the nanofractals.[28] First, we evaluate the Au prepared platforms with 90 s thermally annealed at 400°C for 30 min, the FESEM image revealed very well distributed Au nanodots on the PMMA. The template facilitates the appropriate decoration of Au particles on PMMA without any defects, discontinuities, or local stress. Further clarification was observed in the inset titled image shown in Figure 2 having homogeneous and uniformity in size and structure. The titled images were taken at 45° angle. The diameter of PMMA nanohemisphere was measured to be between ~470 and 490 nm in size as exact replica of the phosphoric concavities.

For the 120 s Au sputtered samples, thermally annealed at the same temperature as the 90 s Au sputtered samples (400°C–30 min), minimal difference in size and distribution is observed in the resulting nanoparticles, however they present increased interspaces compared to the 90 s prepared templates, as illustrated in Figure 2. As mentioned earlier, the resultant fractals are strongly dependent on the sputtering time and thermal treatment followed by substrate morphology. The particle size varies with sputtering time having larger interparticle distances with great uniformity in distribution in size. The inset image in Figure 2 for 120 s clearly revealed the homogeneity of the resultant structure attached to the PMMA surface.

In the next step of the preparing platforms, we followed the exact steps to prepare the platforms but with Ag as a deposited metal with varying sputtering time and thermal treatment. Here, one important point is that the extraction of the nanodots from the nano concavities to the PMMA layer also depend on the PMMA concentration in toluene.

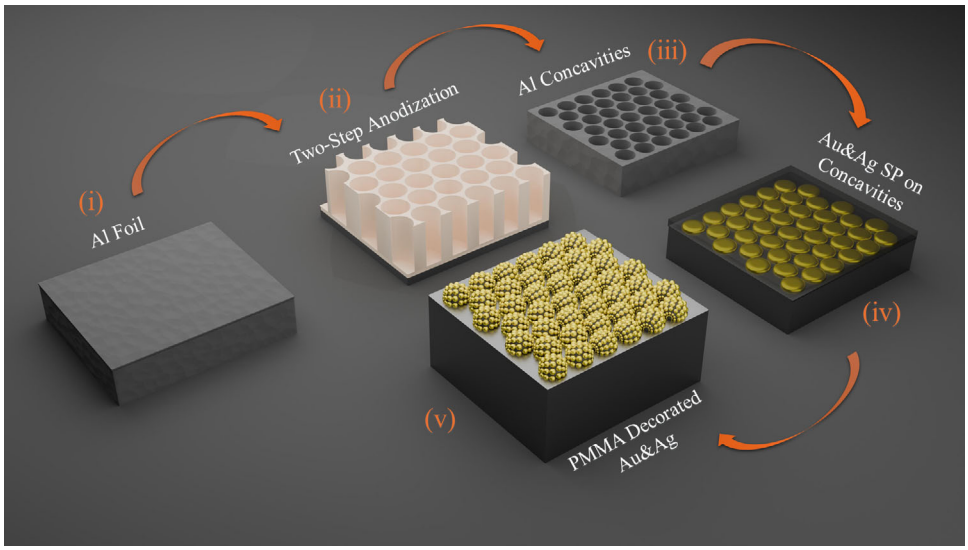

SCHEME 1 Illustration of the fabrication steps of gold and silver nanodot polymethyl methacrylate (Au&Ag_ND-PMMA) template-based protocol and transfer to PMMA: (i) aluminum foil, (ii) nanoporous anodic alumina layer formed after two-step anodization, (iii) aluminum concavities after chemical etching of nanoporous anodic alumina, (iv) Au&Ag deposition layer on aluminum concavities with thermal annealing, and (v) formed Au&Ag_ND transferred to PMMA membrane.

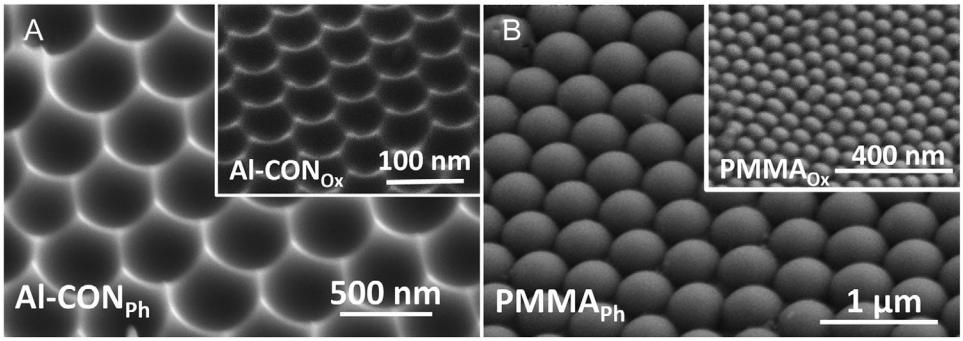

FIGURE 1 (A) Al concavities prepared through phosphoric (Al-CON$_{Ph}$) and oxalic acid (Al-CON$_{Ox}$)—(inset). (B) Polymethyl methacrylate (PMMA) hemisphere without any metal deposition transferred from phosphoric (PMMA$_{Ph}$) and oxalic (PMMA$_{Ox}$) concavities—(inset).

The increased viscosity resulting from a higher concentration of PMMA allows for more NPs to adhere to the PMMA film. However, an excessive amount of PMMA leads to the NPs becoming embedded inside the PMMA film, hence decreasing the efficacy of SERS enhancement. The influence of the PMMA concentration toward the extraction of the NP to PMMA film is revealed in Figure S1. The extraction of the NPs was poorly achieved as compared to the 20% of PMMA in toluene. The FESEM images revealed the extraction of the Ag NPs from Au-equipped Al nano concavities shown in Figure 2. These prepared platforms were varying in sputtering time and thermal treatment as compared to Au. The sputtering time of Ag was 150 and 200 s and thermally annealed at 200°C–15 min. The formation of the resultant particles is well homogeneous and uniform in size. The inset titled images more clarify our observations for distribution and extraction of the NPs from Ag-equipped Al nano concavities. Hence, in the 200 s of Ag sputtering, the particle size and interparticle distance was larger and showing some gaps up to some extent at some places on PMMA-HRs.

We mentioned before that we prepared the two various concavities by employing phosphoric and oxalic acids as electrolyte to observe the particle formation distribution and extraction to the PMMA film. We deployed the Au and Ag sputtering with same time and thermal treatment on the Al concavities prepared through oxalic acid. The FESEM showed the extraction of Au nanofractals onto PMMA film for 90 and 120 s, respectively. In contrast to phosphoric acid, the resulting particles exhibit variations in size and distribution across the PMMA-HRs. There are various small particles attached to the one hemisphere

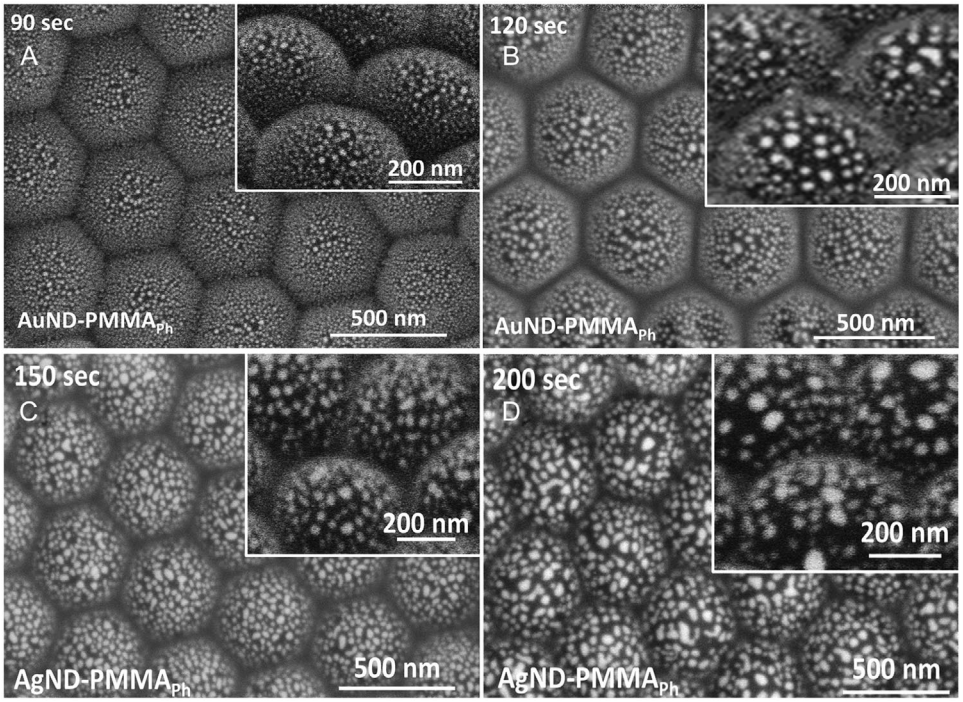

FIGURE 2 Polymethyl methacrylate (PMMA) hemispheres transferred from phosphoric acid concavities Au-nD-PMMA dressed with Au for 90 and 150 s followed by thermal annealing of 400°C–30 min. PMMA Hierarchical structures transferred from phosphoric acid concavities with Ag-nD-PMMA for 150 and 200 s followed by thermal annealing of 200°C–15 min, respectively.

surface in 90 s templates, but in 120 s sputtering FESEM revealed the larger particles mostly one particle on one hemisphere shown in Figure 3. The inset images showed the tilted image taken at 45° to explore more views of the distribution and attachment of the particles on PMMA surface. The observation indicates again that the formation of the particles strongly depends on the morphology of the template. We observed more interparticle space in the 120 s sputtering case because the particle aggregated to form one big particle onto one PMMA hemisphere rather than to spread on other sites. These both prepared platforms were thermally treated at same temperature (400°C–30 min). The bottom part of Figure 3 revealed the formation and distribution of the Ag nanodots after 100 and 150 s sputtering followed by thermally annealed at 200°C–15 min. The resultant size and distribution of Ag nanofractals are showing different behavior for their distribution and size.

Upon subjecting the Au-coated honeycomb-like nanoarrays to heat annealing, the Au layer begins to interact with the surface features of the produced nano concavities. During the sputtering process, the annealing process causes the formation of bigger and evenly distributed gold nanodots on the inner side of the nano concavities. This is owing to the proximity of the particles. The deposition method and thermal annealing treatment were iterated with different parameters to attain the desired augmentation in particle size and reduction in interparticle distance. To achieve interparticle plasmon coupling, it is essential to decrease the distance between particles. This coupling enhances the strength of the near field, perhaps resulting in an enhanced SERS signal or increased sensitivity of the LSPR to variations in refractive index. The quantitative EDS analysis of the prepared platforms is shown in Figure S1.

Various larger Ag formed particles were observed in both cases along with aggregation of the smaller particles as well. So, bunches of particles with various sizes are observable in both cases, which is in contract with Au-formed particles distribution. These types of inhomogeneous size distribution also affected the SERS signals. The growth rate of the Ag as compared to Au could be influenced by various factors after thermal annealing treatment. (1) Crystal structure and diffusion: Despite both gold (Au) and silver (Ag) possess identical face-centered cubic (FCC) crystal structures, the atomic diffusion of Au is slower than that of Ag, resulting in more rapid grain development due to the latter's superior diffusion rate.[29] (2) Grain boundary energy: Au and Ag exhibited opposite grain energy boundaries; Au has higher energy and Ag manages the lower energy grain boundaries that contribute to higher grain growth as compared to Au.[30] (3) Surface energy and diffusion: Ag has slower surface energy allowing atoms to migrate easily with faster grain boundary movement, while for Au surface energy is higher and limiting surface diffusion promotes slower grain growth.[31] (4) Grain size distribution: Au grains growth

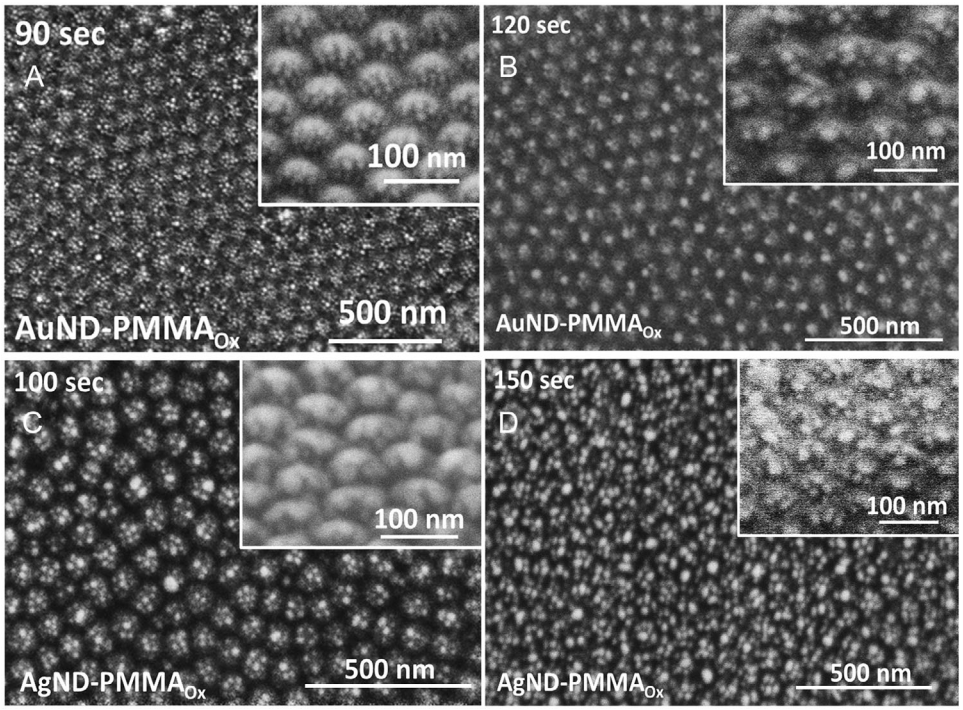

FIGURE 3 Polymethyl methacrylate (PMMA) hemispheres transferred from oxalic acid concavities Au-nD-PMMA dressed with Au for 90 and 150 s followed by thermal annealing at 400°C for 30 min. PMMA hierarchical structures transferred from phosphoric acid concavities with Ag-nD-PMMA for 100 and 150 s followed by thermal annealing at 200°C for 15 min, respectively.

is slower than the Ag grains growth because of its faster growth rate after thermal annealing. These factors collectively influenced the resultant nano fractals depending on how metals react to thermal annealing parameters.[32] Therefore, based on our previous article based on Au dressed on aluminum nano concavities, we experienced that the formation of Au nanopatterns are achieved at 400°C–30 min to get the optimal results for formation of particles with more homogeneity and distribution.[33] On the contrary, we experienced multiple experiment steps to achieve the homogeneous distribution of Ag nanopatterns on Al nano concavities to transfer them to PMMA. We conducted multiple sputtering times and thermal treatments on substrates prepared using oxalic and phosphoric acids to get a homogenous morphology for SERS platforms.

Figure S2 shows the PMMA-HRs transferred from both Al concavities oxalic and phosphoric acids followed by Ag sputtering of 200 s and thermal annealing at 100°C for 30 min, respectively. The distribution of the prepared nanodots was not homogeneous and aggregated on PMMA surface in both cases (oxalic and phosphoric). A larger and red-shifted plasmon resonance is characteristic of smaller NPs, usually ranging from 10 to 50 nm. This change takes place because, as particle size lowers, the LSPR frequency reduces. On the other hand, plasmonic peaks that are smaller and blue-shifted are more common for NPs bigger than 100 nm. The amplification of electromagnetic fields has been reduced in larger NPs due to their lower surface-to-volume ratio. The dispersion of NPs on the substrate significantly influences the uniformity and strength of the SERS signal. A uniformly distributed NP layer ensures that electromagnetic fields are evenly allocated across the surface, resulting in consistent amplification at various measurement points. Nonetheless, aggregated particles might result in localized acceleration in certain areas, producing exceptionally powerful Raman signals while compromising the repeatability and homogeneity of the observations.[34]

This low temperature is still not feasible to achieve the desired structure for SERS activity. Furthermore, we investigated the sputtering time variation of 100 s and thermally annealed at 200°C–15 min; Figure S3 shows the resultant morphology after transferring of nanodots on PMMA-HRs. Figure S3A shows the formation of Ag nanodots on PMMA-HRs transferred from phosphoric concavities with less number and low homogeneity. There was a large gap between Ag nanodots and the PMMA surface was not fully covered, which was not suitable for sensitive SERS activity. Conversely, Figure S3B demonstrated that the large particles formed on the PMMA surface, transferred from the oxalic concavities, appear unattached to the PMMA surface. The formation of the particles is totally opposite to the phosphoric sample. In next preparation, we varied the Ag sputtering time up to 400 s and thermally treated at

200°C for 30 min. Figure S4 shows the FESEM images of morphological characterization of transferred nanopatterns from both platforms (phosphoric (a) and oxalic (b)). At this temperature, high sputtering time tends to aggregate the particles and irregular structure on surface leads to undesired morphology for SERS activity. As in our observation, we measured that 90 s sputtering with 200°C–15 min for phosphoric platforms is a potential parameter to get the fascinating structure on PMMA surface. The same 90 s sputtering duration was mantained while the thermal annealing temperature changed to 300°C for 30 min. The FESEM pictures of these templates (Figure S5A,B) reveal the inadequate distribution and creation of particles. We easily observed that the particles are not formed and seems to be tiny dust particles of Ag, an unfruitful result to further proceed for SERS activity. Consequently, further investigations were done to get the potential morphology for SERS platforms; in Figures S6 and S7, FESEM images revealed the formation and distribution of particles on PMMA surface. The aggregation of Ag particles in Figure S6 is different in both phosphoric and oxalic case and undesired. Further, Figure S7 shows some better results as compared to others thermally annealed at 300°C for 15 min. Phosphoric platforms with 150 s (Figure S7A) and oxalic platforms with 100 s (Figure S7B) show the formation of particles with smaller size and low homogeneous in distribution. The interparticle distance between the formed particles was much larger, which was not feasible for SERS measurements. These all-reported structures on PMMA surface were not desired morphology for SERS activity causes to absence of hot spots for sensitive detection due to their inhomogeneous distribution and attachment to PMMA.

These parameters influenced the growth rate of gold (Au) and silver (Ag). Au demonstrates exceptional plasmonic behavior in smaller grains, making it more desirable for imaging, sensors, and surface-enhanced Raman spectroscopy (SERS) than Ag. The Au and Ag nanodots are attached to PMMA because of several forces' contribution and interactions such as Van der Waals forces, playing a key role to contribute initial attachment for adhesion of NPs.[35] Physical contact and pressure involve stamping or deposition, and physical pressure ascertain the intimate link between PMMA surface and nanodots. Further factors are also responsible for this contact depending upon the preparation like stabilizing agents and ligands, hydrophilic and hydrophobic interactions, chemisorption and surface functional groups, and electrostatic interactions.[36–38] UV-Vis spectroscopy is key tool to characterize the optical properties of Au and Ag nanofractals attached to the PMMA surface. The surface plasmon resonance (SPR) peak for gold nanoparticles (AuNPs) is often observed in the visible region at approximately 520 nm, which corresponds to SPR results from collective oscillations of conduction electrons, as shown in Figure 4A, for all prepared platforms with various sputtering time for both phosphoric and oxalic acids. Consequently, Figure 4B revealed the UV spectrum for PMMA platforms prepared from Ag sputtering showing the broad peaks from 400 to 450 nm. The difference between the vibrational and rotational levels is dynamic and fluctuating. Moreover, electronic transitions are associated with rotational and vibrational alterations, giving rise to UV-VIS spectroscopy. As a result, absorption does not happen at a single wavelength but rather across a spectrum. As a result, the absorbance versus wavelength plot takes on the appearance of a normal Gaussian distribution, completely with a broad peak.[39] NPs of gold and silver can be better understood and used when their UV-Vis curves are plotted, since they show their distinctive optical signatures. NPs of gold (Au) and silver (Ag) have SPR peaks in the defined band, which amplify electromagnetic fields in their immediate vicinity to make clear path for SERS measurements.

By attaching gold nanodots to the surface and along the edges of PMMA-HRs, "super-lenses" can be formed, which act as nano-concentrators and resonant amplifiers for the incident radiation. In the Mie theory, surface plasmons are defined as the aggregate oscillation of free conduction electrons generated by the incident light's oscillating electromagnetic field.[40]

The particles distribution curve of prepared platforms is exhibited in Figures S8 and S9 for both Au and Ag with electrolyte preparations of phosphoric and oxalic acid. The only platforms were measured, which are further employed to get SERS promising results.

2.2 | SERS measurements of RhB

To evaluate the SERS performance of prepared PMMA dressed by Au&Ag nanofractals, we selected the RhB as a probe analyte on the SERS templates. We used various concentrations of RhB from 10^{-2} M up to 10^{-8} M, starting from the Au-dressed PMMA (Au_PMMA) platforms owing to various sputtering time of 90 and 120 s referring to phosphoric acids. These platforms were treated at 400°C–30 min dropping the RhB solution and waiting to dry completely. It is important to note that measurements on the engineered substrates based on PMMA were performed in the dry phase. Since PMAA is a hydrophobic material, when the substrate is exposed to a drop of analyte, most of the target molecules will not directly interact with the deposited metal on the surface of the substrate. This will have an impact on the detection due to air/water interface, and poor analyte adsorption may result in inefficient

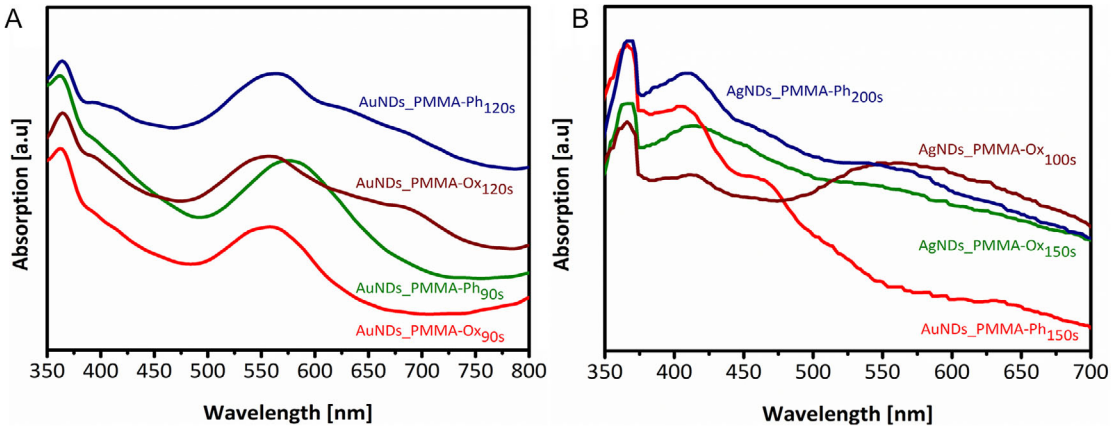

FIGURE 4 UV visible absorption spectra of phosphoric and oxalic acid (A) Au substrate thermally annealed at 400°C for 30 min. (B) Ag prepared platforms thermally annealed at 200°C for 30 min.

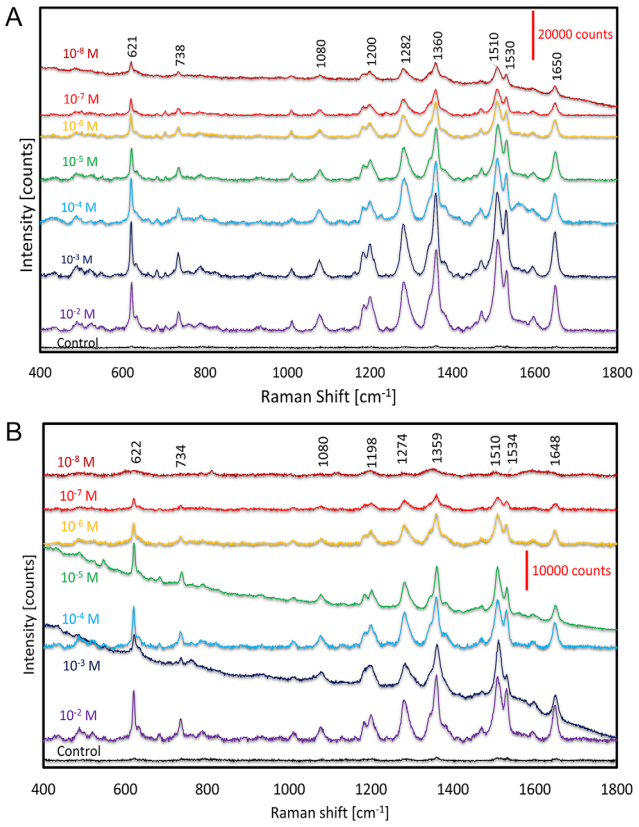

FIGURE 5 Surface-enhanced Raman scattering (SERS) spectra obtained from Au-dressed polymethyl methacrylate (PMMA) hierarchical structures extracted from platforms prepared from phosphoric acid for (A) 90 and (B) 120 s sputtering followed by thermal annealing at 400°C–30 min.

detection.[41] Conversely, although RhB is highly soluble in organic solvents such as ethanol, this liquid matrix cannot be used because organic solvents damage the PMMA layer.

Figure 5A (90 s) and B (120 s) shows the measurements of the RhB spectra of various concentrations. There is a

TABLE 1 The identification of the peaks that are potentially found in the surface-enhanced Raman scattering (SERS) spectra of rhodamine B.

Literature and current work RhB Raman shift (cm^{-1})					
Literature				Present work	Tentative assignments
608	622	613	622	621	C_X–C_X–C_X bend
770	763		732	740	C_X–H out of plane bend
	1075		1075	1080	C_M–H bend
1182		1195	1192	1200	C_X–C_X bend stretching
	1277	1278	1278	1280	C_X–O–C_X stretching
1360	1355	1355	1355	1360	C–N bend stretching
1505	1504	1504	1503	1510	C = C stretching
	1526	1525		1530	C = C stretching
1651	1644	1644	1642	1650	C_X–C_X bend stretching

robust correlation between molecule concentration and Raman intensity. Multiple reports state that a low Raman intensity was caused by improper adsorbed molecules at very low concentrations on the substrate. The modest Raman signal is amplified by the aggregation of the Au NPs at high concentrations. A concentration of RhB 10^{-8} M on the PMMA-HRs may be ideal for SERS activity, since the PMMA surface is protected by the Au&Ag_ND. The Raman signal disappears when the laser light is redirected away from these aggregates because of their low surface concentration. The band assignment for RhB is described in Table 1. All identified bands are well matched with various previous reposts.[42–44] RhB possesses a xanthene ring, which is a structure consisting of an aromatic ring. The surface π-electron clouds of AuNPs or silver nanoparticles (AgNPs) can engage in interactions with the π-electron clouds of aromatic rings. The metal NPs enhance the binding of RhB through a π–π stacking interaction. RhB

possesses multiple vibrational modes that are linked to its molecular structure. RhB possesses multiple vibrational modes that are linked to its molecular structure. C–C and C–N stretching modes are responsible for carbon-carbon (C–C) and carbon–nitrogen (C–N) bonds. C–H bending modes committed of carbon–hydrogen (C–H) bonds. The twisting of C–N–C bond angles are referred to as C–N–C torsional modes. N–H bonding modes involve the nitrogen–hydrogen (N–H) bonds bending. Moreover, ring breathing modes correlate with aromatic rings vibrations in RhB. These modes consider the bending, twisting, and twisting of chemical bonds. The "X" stands for the xanthene ring, the "M" stands for the methyl group, and the "E" stands for the diethylamino group. We observed the various bands near 622 cm^{-1} because of the C_C_C stretching vibration and 738 cm^{-1} corresponding to Cx–H out of plane bend. The bands near 1075 cm^{-1} refers to C_M–H bend stretching, bands near 1182–1200 cm^{-1} correspond to C_X–C_X bend stretching, bands closed to 1278 cm^{-1} correspond to C_X–O–C_X stretching, and bands near 1360 cm^{-1} correspond to the C–N bend stretching. The peak assignments of the aromatic C–H bending range from 1507–1555 cm^{-1}. The SERS peak position closed to 1650 cm^{-1} referred to aromatic C–C bending and C = C stretching vibration. It is implied by this phenomenon that the molecule's spatial orientation changes with respect to the platforms, and that charge transfer enhancement takes place between the surface of the molecule and the substrate. The described assignment bands were observed in all prepared platforms with high and low amplifications signals depending on sputtering time and thermal annealing treatment both for Au&Ag.

In Figure 5, the RhB corresponding SERS peaks are well defined with high amplifications in signals. The minimum detectable concentration in both Au-decorated platforms was 10^{-8} M, and the peak at 1360 cm^{-1} was higher for 90 s than for 120 s. Prior studies have shown that the Raman intensity is low because of its inefficient adsorption and adherence to the Au surface at low concentrations. Additionally, at high concentrations, it tends to agglomerate. To find the optimum platforms for SERS activity to detect the RhB, we measured every single substrate prepared including both phosphoric and oxalic acids owing to various concentrations. Consequently, in Figure 6, the SERS activity was measured through platforms prepared using oxalic acids followed by Au sputtering of 90 and 120 s, respectively. The platforms morphology of both platforms showed the different results of particles morphology formed on PMMA surface. The optimal concentration of RhB in 90 s case was 10^{-8} M, while for 120 s the optimal detecting concentration observed was 10^{-6} M. There was a noticeable difference in the structure of the nanodots generated with oxalic acid for 120 s compared to that for

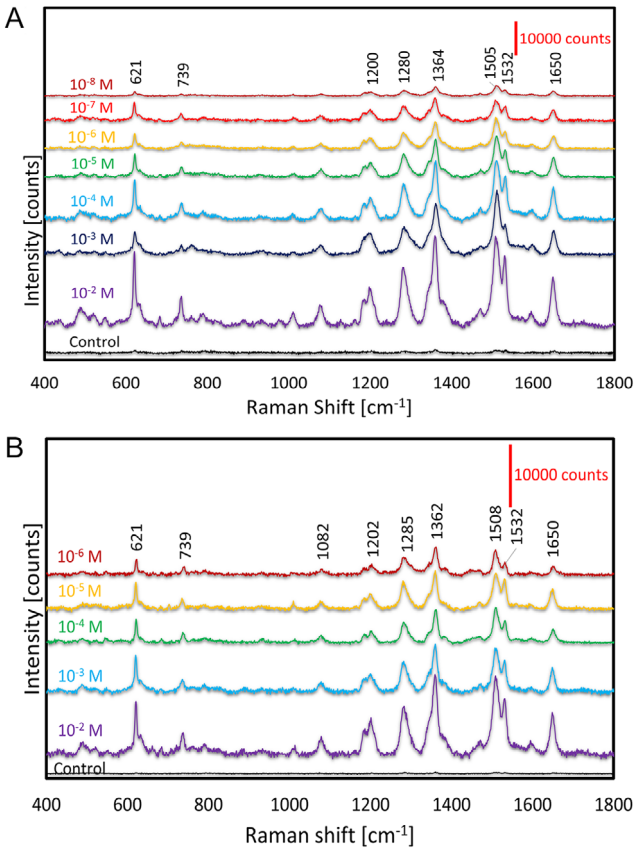

FIGURE 6 Surface-enhanced Raman scattering (SERS) spectra obtained from Au-dressed polymethyl methacrylate (PMMA) hierarchical structures extracted from platforms prepared from oxalic acid for (A) 90 and (B)120 s sputtering followed by thermal annealing at 400°C–30 min.

90 s; the distribution of NPs is much more dispersed, with considerable interparticle distances. These slight modifications occur because the Au nanodots grown on the various platforms have different geometries, which cause them to scatter light to varying degrees and amplify the SERS signals in diverse ways.

Investigating the SERS activity of platforms prepared through Ag sputtering was a little bit challenging in terms of platforms morphology and particles distribution. We altered the sputtering time and thermal annealing treatment to get the well homogeneous structures on PMMA layer. We used the same concentrations of the RhB as for other platforms prepared by Au sputtering up to 10^{-8} M shown in Figure 7.

Ag sputtering of 150 s revealed the SERS peaks with good amplifications up to 10^{-8} M. The morphology of substrate was well homogeneous and capable of adsorption of RhB molecules. In contrast to 150 s, for Ag at 200 s, the optimal RhB concentration was observed to be 10^{-6} M. Consequently, we measured the remaining prepared platforms from oxalic acid followed by Ag sputtering of 100 and 150 s, respectively. The peaks in Figure 8 indicate that

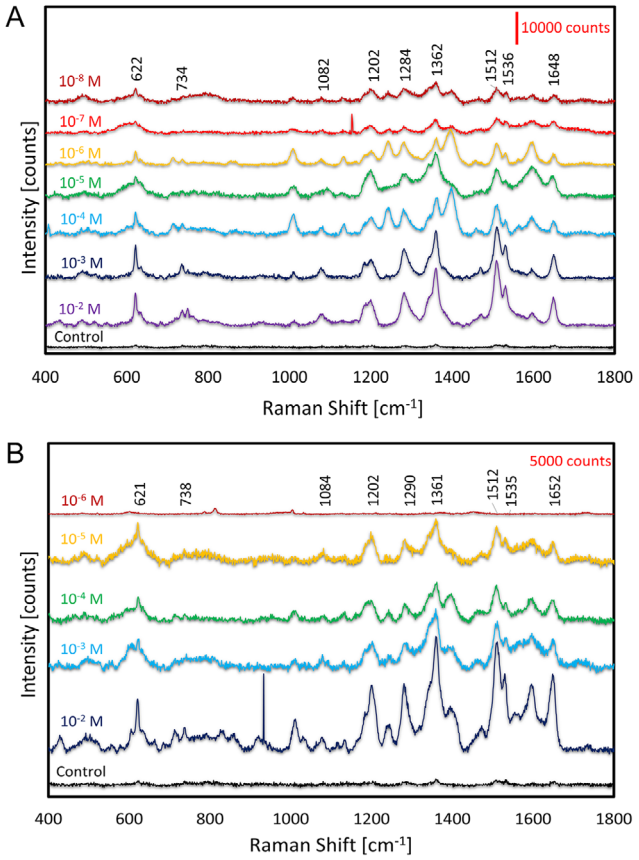

FIGURE 7 Surface-enhanced Raman scattering (SERS) spectra obtained from Ag-dressed polymethyl methacrylate (PMMA) hierarchical structures extracted from platforms prepared from phosphoric acid for (A) 150 and (B) 200 s sputtering followed by thermal annealing at 400°C–30 min.

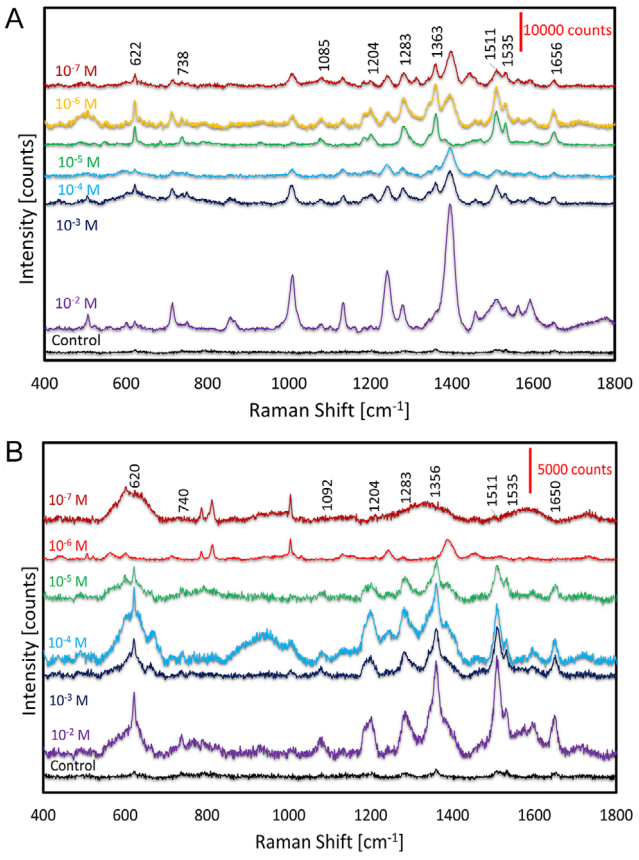

FIGURE 8 Surface-enhanced Raman scattering (SERS) spectra obtained from Ag-dressed polymethyl methacrylate (PMMA) hierarchical structures extracted from platforms prepared from oxalic acid for (A) 100 and (B) 150 s sputtering followed by thermal annealing at 400°C–30 min.

the developed platforms presented a lower detectable concentration of RhB, particularly at 10^{-7} M. There could be various possible reasons to measure the low SERS signal for platforms prepared with PMMA. Figure 9 shows the linear fitting curves obtained between signal intensity and the concentration of the developed substrates for phosphoric and oxalic acid. In contrast to platforms made with Au, those with Ag showed lower SERS signals. This could be due to several factors, like the large distance between the NPs and the RhB molecules, which means that the enhancement is likely to be lower. Additionally, the correct adsorption of molecules is crucial for signal enhancement. PMMA refractive index can influence signal enhancement due to larger interparticle distance and more PMMA surface exposed to laser. The greater the distance between particles, the larger the PMMA area exposed to the laser, which absorbs scatter light and may interfere the measurements. We got some extra peaks in our measurement because of the possibility of PMMA interacting with RhB molecules, resulting in the disturbance of their vibrational modes. The SERS mapping was recorded by selecting the Raman shift 1360 cm^{-1} for best platforms owing to 90 s with highest EF of Au sputtering thermally treated at 400°C–30 min.

2.3 | Enhancement factor

To determine the sensitivity of prepared PMMA platforms, the SERS enhancement factor (EF) is evaluated by using Equation (1).[45]

$$EF = (I_{surf}/N_{surf})\,(I_{bulk}/N_{bulk}) \quad (1)$$

The calculated enhancement factor for Au 90 s substrate prepared through phosphoric acid thermally treated at 400°C–30 min is ~1.2×10^7 (peak 1360 cm^{-1} for 10^{-8} M concentration) and ~9.0×10^6 (peak 1510 cm^{-1} for 10^{-8} M concentration). To evaluate the substrate prepared from oxalic acid followed by 90 s Au sputtering thermally treated at 400°C–30 min, the EF calculated was ~3.8×10^6 (peak 1360 cm^{-1} for 10^{-8} M concentration) and 4.3×10^6 (peak

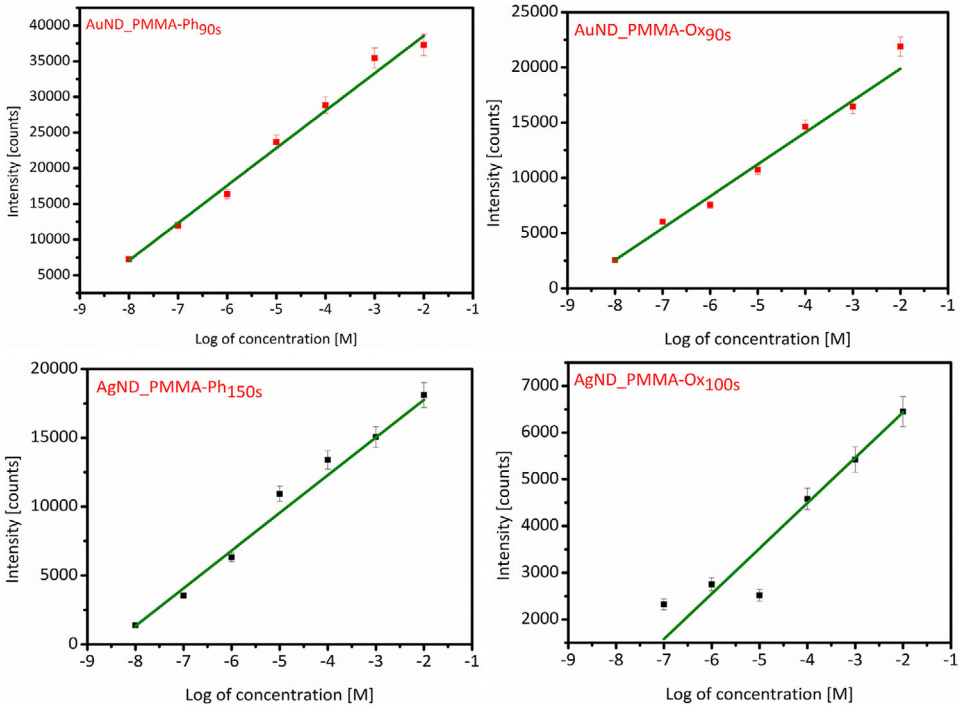

FIGURE 9 Linear fitting curve (green) between signal intensity and concentration of prepared substrate for phosphoric and oxalic acid with high EF (value of the Raman shift evaluated 1360 cm^{-1}), indicating the quantification region.

1510 cm^{-1} for 10^{-8} M concentration), respectively. Furthermore, for platforms prepared through phosphoric acid followed by Ag sputtering of 150 s thermally annealed at 200°C–15 min, the EF calculated was $\sim 7.0 \times 10^6$ (peak 1360 cm^{-1} for 10^{-8} M concentration) and $\sim 8.2 \times 10^6$ (peak 1511 cm^{-1} for 10^{-8} M concentration). The platforms prepared through oxalic acid followed by Ag sputtering of 100 s thermally annealed at 200°C–15 min, the EF calculated was $\sim 5.7 \times 10^5$ (peak 1360 cm^{-1} for 10^{-7} M concentration) and $\sim 4.6 \times 10^5$ (peak 1510 cm^{-1} for 10^{-7} M concentration). We recognize that the sensitivity of our SERS substrate (10^{-8} M) is inferior to that of certain other studies utilizing templated or self-assembled methods, which can attain detection limits ranging from 10^{-9} to 10^{-20} M.[46–53] Our research concentrates on PMMA substrates, which, despite differing in surface chemistry and morphology from SiO_2-based, ZnO substrates, present benefits in fabrication simplicity, reproducibility, and cost efficiency, which are crucial for practical sensing applications, especially in biosensing.[47,48] Our target analyte is rhodamine B (RhB), which can interact with silver and gold through carboxylate groups, and other lone pair donating sites might be nitrogen atoms, which can sometimes lead to competitive binding and aggregating of molecules as compared to other analytes such as Rhodamine 6G and methylene blue. Furthermore, for many analytes, our 10^{-8} M sensitivity is still competitive; however, sensitivity could be increased with additional substrate design and NP distribution optimization. Our method offers substantial SERS enhancement for detection at relatively low concentrations while concentrating on practicality and scalability for real-world applications, in contrast to templated or self-assembled systems that can give exceptionally high sensitivity.

The EF calculation of all prepared platforms with respective peaks is presented in Table 2. Several prior investigations have documented the presence of hollow AuNPs and chemically altered AuNPs on diverse surfaces. These NPs likewise exhibit the distinct Raman peaks of RhB, although their locations may vary. Nevertheless, these platforms are inherently unstable and challenging to consistently acquire in contrast to the deposition of AuNPs via the sputtering process. In our measurements, the optimal concentration was 10^{-8} M followed by the potential platform Au sputtering of 90 s with thermal treatment at 400°C for 30 min. The reason for this optimum Raman response is due to the upper Au nanodots formed during the thermal annealing and transferred to PMMA, which make their maximum contribution to the scattering of most of the light for the enhancement of SERS activity. (1) Wide-ranging synthesis: The lateral dimensions of the substrate are unrestricted, enabling the fabrication of sensors with extensive surface areas and homogeneous dispersion of NPs over the surface. Substantial sensor areas play an important role for LSPR imaging (LSPRi) and SERS.[60,61] (2) Precise fabrication: Efficient modulation of particle size and spacing in a uniform hexagonal

TABLE 2 Evaluation of prepared platforms with associated Raman shifts and enhancement factors (cm^{-1}).

Acid	Metal	Sputtering time (s)	Thermal annealing	Raman shift (cm^{-1}) and RhB concentration	EF
H_3PO_4	Au	90	400°C–30 min	1360 cm^{-1} for 10^{-8} M	1.2×10^7
H_3PO_4	Au	120	400°C–30 min	1198 cm^{-1} for 10^{-8} M	2.2×10^6
$H_2C_2O_4$	Au	90	400°C–30 min	1505 cm^{-1} for 10^{-8} M	4.3×10^6
$H_2C_2O_4$	Au	120	400°C–30 min	1508 cm^{-1} for 10^{-6} M	1.1×10^4
H_3PO_4	Ag	150	200°C–15 min	1512 cm^{-1} for 10^{-8} M	8.2×10^6
H_3PO_4	Ag	200	200°C–15 min	1362 cm^{-1} for 10^{-6} M	2.2×10^4
$H_2C_2O_4$	Ag	100	200°C–15 min	1363 cm^{-1} for 10^{-7} M	5.7×10^5
$H_2C_2O_4$	Ag	150	200°C–15 min	1363 cm^{-1} for 10^{-7} M	3.1×10^5

TABLE 3 Comparative analysis of the enhancement factor (EF) of the surface-enhanced Raman scattering (SERS) substrate with alternative reported platforms.

Metal and substrate	Probe molecule	Enhancement factor	Ref.
Au nano cubes/PMMA	R6G	1.4×10^4	[54]
2D ($PdSe_2$) dendrites	RhB	10^5	[55]
Graphitic carbon nitride@Ag	RhB	3.2×10^6	[56]
Psi/MoS_2/Au	R6G	6.5×10^7	[57]
PMMA/ZnO–Ag	MB	6.3×10^5	[58]
Plasma-treated graphene	RhB	1.3×10^4	[59]
Au&Ag-dressed PMMA	RhB	1.2×10^7	Present

arrangement enables precise adjustment of the plasmonic absorption peak and sensitivity for targeted applications. Optimizing the absorption peak is crucial for surface-enhanced Raman scattering SERS applications, since the correlation between the resonance peak of the substrate and the excitation wavelength of the laser contributes to the amplification of SERS.[62] (3) Adequate robustness: The Au&Ag_ND that were synthesized and deposited onto PMMA hemispheres demonstrate impeccable stability in the configuration of nanodots. Particle removal does not take place in fluidic environments. Repeatedly purifying the surface of PMMA using ultra-pure water does not result in a significant decrease in apparent strength. The existence of Au&Ag_ND-PSLs on PMMA platforms, along with this highly enrichment approach, shows great promise for improving SERS detection.

Table 3 is a compilation of the analytical performances and morphological methodologies used in the development and applications of SERS, which is a rapidly advancing and dynamic field. Signal strength may vary across measurements, as has been observed in other types of heterogeneous SERS platforms and analytes with different concentrations. The quantity of Raman probe molecules that adhere to the nanostructures in complex and heterogeneous platforms might significantly fluctuate based on the geometrical and morphological characteristics of the platforms. The results of our study clearly demonstrate that by adjusting Ag NP size, shape, and distribution on PMMA, SPRs can be tuned and the developed platforms outperformed other references in terms of their ability to detect RhB. Other substrates may be less tunable for certain analytes or experimental conditions. The biocompatibility of PMMA-based SERS substrates makes them appropriate for detecting biological and environmental materials in biomedical applications, especially in biosensing, unlike SiO_2, ZnO nanoplates, and glass substrates, demonstrating superior SERS performance which may require surface modification for bio-detection.[47,48] This was determined by directly comparing all published SERS peaks and their corresponding enhancement factor values.

3 | CONCLUSION

In conclusion, our work shows that Ag/Au nanodots dressed on PMMA layer of varying sizes and compositions may be synthesized via a simple procedure that includes sputtering, heat annealing, and substrate recurrence. This method worked well and produced usable results; by adjusting the times of sputtering for Ag and Au and thermal annealing, we were able to manage the homogeneity in size and distribution. As the sputtering period of Ag/Au varies, the absorption peaks show changes that correspond to changes in particle size and distribution. Therefore, the co-reduction process offered a versatile and appropriate method for creating Au/Ag nanodots with controllable sizes and various compositions. The Ag/Au nanodots were extracted in an ordered and homogeneous manner, making them suitable for use as a SERS substrate. The extraction process resulted in good reproducibility and strong SERS activity. The gold nanodots on PMMA demonstrated the highest performance in SERS when excited at a wavelength of 785 nm. The tailored active SERS substrate is advantageous for the

highly sensitive detection of RhB molecules. The SERS measurements conducted on the RhB solution indicated that the Au/Ag nanodots demonstrated a high level of SERS performance with EF of 10^7. Apart from RhB, any molecule that is likely to be detected by Raman can be detected with the PMMA-based substrates like antibiotics (ciprofloxacin, tetracycline, amoxicillin, etc.), probe molecules (4-mercaptopyridine and mercaptobenzoic acid), dyes (crystal violet, malachite green, rhodamine 6G), and many others that could be object of interest. Due to their appealing characteristics, such as a practical manufacturing process and straightforward detection, the Au/Ag nanodots dressed on PMMA have the potential to be an ideal choice for utilizing SERS in environmental monitoring, food safety investigation, and the quick identification of RhB.

4 | EXPERIMENTAL

4.1 | Materials

Aluminum foils (99.9997% purity and 0.32 mm thickness) were acquired from Goodfellow in Cambridge, UK. Sigma-Aldrich supplied PMMA, phosphoric acid (H_3PO_4; purity 97 %), perchloric acid ($HClO_4$), hydrochloric acid (HCl), chromic acid (H_2CrO_4), ethanol (C_2H_5OH, EtOH), and RhB ($C_{28}H_{31}ClN_2O_3$). Ultrapure water was used to make aqueous solutions.

4.2 | Preparation of Al concavities platforms

The aluminum sheets were first cut into 1.5 × 1.5 cm^2 square platforms. To eliminate surface contaminants, they were washed in ethanol and Milli-Q water in a repeated sequence under sonication for 5 min each. The Al platforms were stored in a dry environment after being air-dried. In order to achieve uniform pore formation without the negative side effects of localized electric fields, Al platforms were electropolished in an electrolyte mixture consisting of 4:1 (v:v) EtOH:$HClO_4$. This process smoothed out their surface roughness. Continual and vigorous stirring was used for 3 min at a potential of 20 V and an electrolyte temperature of around 5°C to carry out this procedure (power supply 0–300 V, 0–5 A, 1500 W). To manipulate the geometric properties of NAA membranes, two separate acid electrolytes were used: 0.3 M oxalic acid and 0.1 M phosphoric acid.

NAA_{Ox} first anodization process was continued for 20 h by adjusting the temperature at 5°C and voltage at 40 V. The formed Al_2O_3 layer was dissolved in a chromic and phosphoric acid solution. Then a second anodization step was performed under identical voltage and temperature conditions for 1 h. NAA_{Ph} initial anodization process consisted of three steps: (i) a 3-h exposure to 175 V and (ii) an 18-h exposure to 195 V with an anodizing voltage increment of 0.005 V s^{-1}. To prevent the aqueous H_3PO_4 acid electrolyte from freezing in frigid conditions, EtOH was mixed into it. After the Al_2O_3 layer was dissolved in a solution of chromic and phosphoric acids, under carefully regulated circumstances, the solution was heated to 70°C for 2 h, with a weight percentage of 1.8% chromic acid and 6% phosphoric acid. As a result of its nanoporous structure, Al_2O_3 dissolved at different rates; its solubility reduced as one moved away from the pores and quickly increased when one was close to them. Following the ethanol washing and drying of the sample, the second anodization stage is conducted for 3 h at the same temperature and applied voltage (195 V) conditions as the first phase. Upon completion of the procedure, a hexagonal arrangement of self-ordered pores of uniform size was noticed in the NAA layer. After combining the NAA platforms with chromic acid (1.8% wt.%) and phosphoric acid (6 wt.%) in a vigorously stirring mixture, they were kept at 70°C for 2 h to obtain the desired hemisphere form on the alloy sheet. Raising the connecting regions of three adjacent concavities in an upright fashion allows one to fabricate an Al concave hemisphere hexagonal structure resembling dimple array.

Electrolytes comprised of oxalic, chromic, phosphoric, or sulfuric acid are used to obtain NAA templates. Different types of electrolytes allow for varying the anodization voltage.[25] After 12 h of anodization, 63, 500, and 100 nm interpore distances can be formed by sulfuric acid at 0.3 M (25 V), phosphoric acid at 0.1 M (150–195 V), and oxalic acid at 0.3 M (40 V). The porosity of the anodized sample is impacted by the temperature changes in the electrolyte. As temperature rises, pores form at a faster rate.[63,64]

4.3 | Formation of Au&Ag nanodots

The hexagonal nano concave Al arrays were utilized to demonstrate the reagent-free generation of Au&Ag fractal patterns. The fabrication of SERS platforms by means of traditional lithography techniques was time consuming, costly, and necessitated the expertise of highly competent operators. In this instance, it was proposed to utilize a treatment that combines thermal annealing and sputtering.

The initial step of developing an Au&Ag layer on the Al nanoconcavities template was to employ a sputtering method to conduct simple reagent-free physical vaporization deposition (PVD). During the PVD process, the target material was heated to a vapor state before being

condensed on the surface of the substrate in a vacuum. In the PVD method, magnetron sputtering used argon ions in plasma to smash high-energy ions against the surface of the substrate, depositing target atoms on the top. Given the target was 99.99% Au&Ag and the parameters were adjusted to 3 mTorr pressure, 20 sccm Ar flow rate, and 30 W Rf power, the BESTEC magnetron sputtering system was mainly employed to deposit an Au thin film. We examined the effect of this parameter on the final substrate by using two alternative sputtering timings and thermal annealing temperatures for Au (90, 120, and 150 s thermally annealed at 400°C–30 min) and Ag (100, 150, and 200 s thermally annealed at 200°C–15 min), keeping all other sputtering parameters constant. After subjecting the materials to thermal annealing for different durations and temperatures, we were able to compare the outcomes as SERS platforms. Over the Al nanoconcavities templates, varying distributions of Au nanodots (NPs) and nano islands were produced by adjusting the sputtering time, annealing time, and temperature.

4.4 | Fabrication PMMA-based platforms

The large-scale fabrication of nanoporous alumina with great accuracy and homogeneity, as well as the tunability of its porosity, average pore size, and pore depth through electrochemical preparation, make it an appealing choice for use as a nano template. Furthermore, self-ordered nanoporous alumina has emerged as a prominent nano template for the fabrication of various structures at the nanoscale. Anodizing long-range-ordered porous alumina to a hexagonal array of nanopores with an optimally uniform arrangement is possible under certain conditions. Nanostructures were prepared by infiltrating a polymer solution into a template while maintaining a vacuum. The acrylic polymer that was selected for this method is PMMA. PMMA is a great option for practical applications and large-scale production because it is inexpensive, lightweight, flexible, and transparent. Metal NP integration on PMMA is also made simply by the template-assisted replica method without any further complex surface functionalization, which preserves stability and repeatability. Its adaptability also benefits several sensing applications, particularly biosensing, where handling simplicity and system integration are essential. Because of its adaptability, this polymer has found use in many different fields and products.

A method for creating PMMA structures using a template was suggested; this method involves placing a solution into the template using vacuum infiltration. The experimental approach comprises heating the sample to evaporate any remaining solvent after penetrating it under vacuum with a drop of PMMA solution in toluene. The aluminum nanoconcvaities membrane served as a template for the infiltration of a 20 wt% PMMA solution into toluene, resulting in the formation of PMMA-HRs. After plating the Al nanoconcavity template with Au NPs, 300 µL of PMMA toluene solution was pipetted onto its surface. The platforms were dried to evaporate the toluene. When the template's cured PMMA layer cooled, anodized part of the Al was carefully dissolved in the solution of $CuCl_2.2H_2O$ (13.6 g) and HCl (100 mL) in DH_2O (400 mL) to get a PMMA-HRs substrate dressed with Au&Ag NDs. Scheme 1 illustrates how Au&Ag NDs are transferred from the nano hemisphere-equipped Al template to the PMMA surface, creating a reconfigurable substrate and the in-situ SERS detection process.

5 | CHARACTERIZATION TECHNIQUES

5.1 | Optical and structural characterizations

The FESEM (model Scios 2) manufactured by Thermo Fisher Scientific is being equipped with a voltage of 5 kV that is increasing in intensity.

To obtain absorbance spectra, a PerkinElmer Lambda 950-UV–vis/NIR spectrometer was employed at room temperature.

5.2 | SERS measurements

To acquire the SERS observations, a Renishaw inVia Raman Microscope confocal spectrometer, a 50× LWD objective lens, and a 1200 lines/mm grating were employed. The apparatus was fitted with a laser that had an excitation wavelength of 785 nm. Although the optical absorption of the PMMA substrate decorated with AgNPs indicates superior compatibility with green light (514 or 532 nm). We selected 785 nm to optimize signal intensity while maintaining substrate stability and reducing fluorescence interference and risk of photo-induced degradation, which tends to be more significant at shorter excitation wavelengths.[65] The most common of the three standard wavelengths, 785 nm, strikes a balance between spectral resolution and fluorescence reduction.

The starting power of the laser was 10 mW, and each substrate was experienced for 10 s before being exposed. The laser point, which measured ~1 µm in diameter, held a spherical shape. It was possible to acquire each of the three successive measurements, and each of the three acquisitions was likely collected from a different location.

5.3 | SERS sensing platforms

As described earlier, we prepared SERS platforms owing two noble metals Au and Ag. These platforms are prepared for various time intervals of magnetron sputtering (Au = 90 and 120 s; Ag = 100, 150, and 200 s). RhB was selected as probe molecules to measure the SERS performance of the Au&Ag-dressed PMMA (Ag_PMMA) platforms under illumination of 785 nm laser. Various amounts of RhB concentrations were utilized from 0.1 to 10^{-8} M. Note that 0.1 M concentration of RhB was referred as control in aqueous solution. Solutions were dropped on the platforms and allowed to dry completely.

ACKNOWLEDGMENTS

This project has received funding from the European Union's Horizon 2020 research and innovation program under the Marie Skłodowska-Curie grant agreement No. 945413 and from the Universitat Rovira i Virgili (URV). This work was supported by the Spanish Ministerio de Ciencia e Innovación (MICINN/FEDER) PDI2021-128342OB-I00, the Agency for Management of University and Research Grants (AGAUR) ref. 2021- SGR-00739, COST Action 20126-NETPORE, and the Catalan Institution for Research and Advanced Studies (ICREA) under the ICREA Academia Award and by the Diputació of Tarragona: (DIPTA) 2022/33. Abel Santos thanks the support provided by the Australian Research Council through the grant DP220102857.

CONFLICT OF INTEREST STATEMENT

The authors declare no conflict of interest.

ORCID

Lluis F. Marsal https://orcid.org/0000-0002-5976-1408

REFERENCES

1. a) H. Li, Q. Yang, J. Hou, Y. Li, M. Li, Y. Song, *Adv. Funct. Mater.* **2018**, *28*, 1870144; b) L. L. Tan, M. Wei, L. Shang, Y. W. Yang, *Adv. Funct. Mater.* **2021**, *31*, 2007277.
2. a) C. V. Di Anibal, L. F. Marsal, M. P. Callao, I. Ruisánchez, *Spectrochim Acta A: Mol Biomol Spectrosc* **2012**, *87*, 135. b) S. Cortijo-Campos, R. Ramírez-Jiménez, A. De Andrés, *Nanomaterials* **2021**, *11*, 644.
3. Q. Yuan, H. Fang, X. Wu, J. Wu, X. Luo, R. Peng, S. Xu, S. Yan, *ACS Appl Mater Interfaces* **2024**, *16*, 66810.
4. M. Nasilowski, B. Mahler, E. Lhuillier, S. Ithurria, B. Dubertret, *Chem. Rev.* **2016**, *116*, 10934.
5. C. García-Astrain, M. Henriksen-Lacey, E. Lenzi, C. Renero-Lecuna, J. Langer, P. Piñeiro, B. Molina-Martínez, J. Plou, D. Jimenez de Aberasturi, L. M. Liz-Marzán, *ACS Nano* **2024**, *18*, 11257.
6. A. Aziz, R. Nauber, A. S. Iglesias, L. M. Liz-Marzán, O. G. Schmidt, M. Medina-Sánchez, Presented at 2022 Int Conf. Manipulation, Automation and Robotics at Small Scales (MARSS), Toronto, ON, Canada, **2022**.
7. D. Wang, J. Hu, G. C. Schatz, T. W. Odom, *J. Phys. Chem. Lett.* **2023**, *14*, 8525.
8. J. Guan, R. Li, X. G. Juarez, A. D. Sample, Y. Wang, G. C. Schatz, T. W. Odom, *Adv. Mater.* **2023**, *35*, 2103262.
9. A. Zdaniauskienė, M. Talaikis, T. Charkova, R. Sadzevičienė, L. Labanauskas, G. Niaura, *Molecules* **2022**, *27*, 6531.
10. a) S. X. Leong, C. S. L. Koh, H. Y. F. Sim, Y. H. Lee, X. Han, G. C. Phan-Quang, X. Y. Ling, *ACS Nano* **2021**, *15*, 1817. b) E. Xifre-Perez, J. Ferre-Borull, J. Pallares, L. F. Marsal, *Open Mater. Sci.* **2015**, *2*, 13.
11. a) R. Ji, W. Lee, R. Scholz, U. Goesele, K. Nielsch, *Adv. Mater.* **2006**, *18*, 2593; b) L. Wang, S. Patskovsky, B. Gauthier-Soumis, M. Meunier, *Small* **2022**, *18*, 2105209; c) V. Brasiliense, J. E. Park, Z. Chen, R. P. Van Duyne, G. C. Schatz, *J. Raman Spectrosc.* **2021**, *52*, 339.
12. S. Dubkov, D. Novikov, H. Bandarenka, A. Burko, A. Trifonov, L. Volkova, P. Edelbekova, E. Lebedev, E. Skryleva, D. Gromov, *Appl. Surf. Sci.* **2024**, *645*, 158682.
13. X. Wang, S.-C. Huang, S. Hu, S. Yan, B. Ren, *Nat. Rev. Phys.* **2020**, *2*, 253.
14. M. S. S. Bharati, V. R. Soma, *Opto-Electronic Adv.* **2021**, *4*, 210048.
15. D. Zhang, H. Pu, L. Huang, D.-W. Sun, *Trends Food Sci. Technol.* **2021**, *109*, 690.
16. X. Dong, X. Yan, Y. Yuan, Y. Xia, T. Yue, *Food Chem.* **2024**, *451*, 139515.
17. Y. Wang, B. Yang, Z. Hua, J. Zhang, P. Guo, D. Hao, Y. Gao, J. Huang, *J. Phys. D: Appl. Phys.* **2021**, *55*, 134001.
18. L. Wang, K. Jiang, G. Shen, *Appl. Phys. Lett.* **2021**, 119.
19. X. Zhao, J. Yu, C. Zhang, C. Chen, S. Xu, C. Li, Z. Li, S. Zhang, A. Liu, B. Man, *Appl. Surf. Sci.* **2018**, *455*, 1171.
20. J. Wang, C. S. Law, S. Gunenthiran, H. N. Que Tran, K. N. Tran, S. Y. Lim, A. D. Abell, A. Santos, *ACS Appl. Mater. Interfaces* **2022**, *14*, 21181.
21. S. Kasani, K. Curtin, N. Wu, *Nanophotonics* **2019**, *8*, 2065.
22. T. Kumeria, A. Santos, M. M. Rahman, J. Ferré-Borrull, L. F. Marsal, D. Losic, *ACS Photonics* **2014**, *1*, 1298.
23. J. Domagalski, E. Xifre-Perez, M. Tabrizi, J. Ferre-Borrull, L. F. Marsal, *J. Coll. Interface Sci.* **2021**, *584*, 236.
24. A. Santos, L. F. Marsal, T. Kumeria, *Front. Chem.* **2020**, *8*, 595931.
25. A. Santos, L. Vojkuvka, M. Alba, V. S. Balderrama, J. Ferré-Borrull, J. Pallarès, L. F. Marsal, *Physica Status Solidi* **2012**, *209*, 2045.
26. H. Ikeda, M. Iwai, D. Nakajima, T. Kikuchi, S. Natsui, N. Sakaguchi, R. O. Suzuki, *Appl. Surf. Sci.* **2019**, *465*, 747.
27. G. A. Vinnacombe-Willson, Y. Conti, A. Stefancu, P. S. Weiss, E. Cortés, L. Scarabelli, *Chem. Rev.* **2023**, *123*, 8488.
28. Z. Chen, Z. Jiao, M. Wu, C. H. Shek, C. M. L. Wu, J. Lai, *Prog. Mater. Sci.* **2011**, *56*, 901.
29. N. A. C. Lah, S. Trigueros, *Sci. Technol. Adv. Mater.* **2019**, *20*, 225.
30. J. Pan, R. Balluffi, *Acta Metall.* **1982**, *30*, 861.
31. F. Baletto, C. Mottet, R. Ferrando, *Surf. Sci.* **2000**, *446*, 31.
32. Z. Zhang, C. Chen, G. Liu, C. Li, S. Kurosaka, S. Nagao, K. Suganuma, *Appl. Surf. Sci.* **2019**, *485*, 468.
33. G. I. Dar, E. Xifre-Perez, L. F. Marsal, *Adv. Mater. Interfaces* **2023**, *10*, 2300560.
34. a) R. X. He, R. Liang, P. Peng, Y. Norman Zhou, *J. Nanopart. Res.* **2017**, *19*, 267; b) O. A. Yeshchenko, I. M. Dmitruk, A. A.

Alexeenko, A. V. Kotko, J. Verdal, A. O. Pinchuk, *Plasmonics* **2012**, *7*, 685.
35. F. Ruffino, V. Torrisi, G. Marletta, M. Grimaldi, *J. Appl. Phys.* **2012**, *112*, 12.
36. E. Palleau, N. Sangeetha, L. Ressier, *Nanotechnology* **2011**, *22*, 325603.
37. E. Yilmaz, G. Ertas, E. Bengu, S. Suzer, *J. Phys. Chem. C* **2010**, *114*, 18401.
38. J. Sun, Z. Li, Y. Sun, L. Zhong, J. Huang, J. Zhang, Z. Liang, J. Chen, L. Jiang, *Nano Res.* **2018**, *11*, 953.
39. M. S. H. Akash, K. Rehman, *Essen. Pharm. Anal.* Springer, **2020**.
40. F. Alzoubi, A. A. Ahmad, I. A. Aljarrah, A. Migdadi, Q. M. Al-Bataineh, *J. Mater. Sci.: Mater. Electron.* **2023**, *34*, 2128.
41. a) X. He, Y. Liu, X. Xue, J. Liu, Y. Liu, Z. Li, *J. Mater. Chem. C* **2017**, *5*, 12384; b) H. Feng, F. Yang, J. Dong, Q. Liu, *RSC Adv.* **2020**, *10*, 11865.
42. C. Sun, M. Wang, Q. Feng, W. Liu, C. Xu, *Russ. J. Phys. Chem. A* **2015**, *89*, 291.
43. Y. Zhao, G. Chen, Y. Du, J. Xu, S. Wu, Y. Qu, Y. Zhu,*Nanoscale* **2014**, *6*, 13754.
44. Y. Ma, L. Yang, Y. Yang, Y. Peng, Y. Wei, Z. Huang, *RSC Adv.* **2018**, *8*, 22095.
45. G. I. Dar, E. Xifre-Perez, L. F. Marsal, *J. Mater. Chem. C* **2024**, *12*, 17305.
46. O. Olea-Mejía, M. Fernández-Mondragón, G. Rodríguez-de la Concha, M. Camacho-López, *Appl. Surf. Sci.* **2015**, *348*, 66.
47. V. Dzhagan, N. Mazur, O. Kapush, M. Skoryk, Y. Pirko, A. Yemets, V. Dzhahan, P. Shepeliavyi, M. Valakh, V. Yukhymchuk, *ACS Omega* **2024**, *9*, 4819.
48. T. T. H. Pham, X. H. Vu, N. D. Dien, T. T. Trang, T. T. K. Chi, P. H. Phuong, N. T. Nghia, *RSC Adv.* **2022**, *12*, 7850.
49. L. Zhou, S. Poggesi, G. Casari Bariani, R. Mittapalli, P.-M. Adam, M. Manzano, R. E. Ionescu, *Biosensors* **2019**, *9*, 53.
50. M. Q. Doan, N. H. Anh, N. X. Quang, N. X. Dinh, D. Q. Tri, T. Q. Huy, A.-T. Le, *J. Electron. Mater.* **2022**, *51*, 150.
51. N. Mazur, O. Kapush, O. Isaeva, S. Budzulyak, A. Y. Buziashvili, Y. Pirko, M. Skoryk, A. Yemets, O. Hreshchuk, V. Yukhymchuk, *Phys. Chem. Solid State* **2023**, *24*, 682.
52. I. Shaikh, M. A. Haque, H. Pathan, S. Sartale, *Plasmonics* **2022**, *17*, 1889.
53. M. L. Coluccio, G. Das, F. Mecarini, F. Gentile, A. Pujia, L. Bava, R. Tallerico, P. Candeloro, C. Liberale, F. De Angelis, *Microelectron. Eng.* **2009**, *86*, 1085.
54. X. Wang, Y. Wu, X. Wen, X. Bai, Y. Qi, L. Zhang, H. Yang, Z. Yi, *Opt. Mater.* **2021**, *121*, 111536.
55. T. Jena, M. T. Hossain, U. Nath, M. Sarma, H. Sugimoto, M. Fujii, P. Giri, *npj 2D Mater. Appl.* **2023**, *7*, 8.
56. Y. Jiang, H. Sun, C. Gu, Y. Zhang, T. Jiang, *Analyst* **2021**, *146*, 5923.
57. X. Zhao, C. Liu, J. Yu, Z. Li, L. Liu, C. Li, S. Xu, W. Li, B. Man, C. Zhang, *Nanophotonics* **2020**, *9*, 4761.
58. S. Karagoz, N. B. Kiremitler, G. Sarp, S. Pekdemir, S. Salem, A. e. G. Goksu, M. S. Onses, I. Sozdutmaz, E. Sahmetlioglu, E. S. Ozkara, *ACS Appl. Mater. Interfaces* **2021**, *13*, 5678.
59. N. S. Singh, F. Mayanglambam, H. B. Nemade, P. Giri, *ACS Appl. Nano Mater.* **2022**, *5*, 6352.
60. I. Kaminska, T. Maurer, R. Nicolas, M. Renault, T. Lerond, R. Salas-Montiel, Z. Herro, M. Kazan, J. Niedziolka-Jönsson, J. Plain, *J. Phys. Chem. C* **2015**, *119*, 9470.
61. P. Singh, *Rev. Plasmonics* **2017**, *211*.
62. R. Pilot, R. Signorini, C. Durante, L. Orian, M. Bhamidipati, L. Fabris, *Biosensors* **2019**, *9*, 57.
63. M. Amouzadeh Tabrizi, J. Ferré-Borrull, L. F. Marsal, *Sci. Rep.* **2020**, *10*, 2356.
64. C. S. Law, S. Y. Lim, A. D. Abell, L. F. Marsal, A. Santos, *Nanoscale* **2018**, *10*, 14139.
65. Y. Hang, J. Boryczka, N. Wu, *Chem. Soc. Rev.* **2022**, *51*, 329.

SUPPORTING INFORMATION

Additional supporting information can be found online in the Supporting Information section at the end of this article.

How to cite this article: G. Dar, E. Xifre-Perez, A. Santos, L. F. Marsal, *VIEW.* **2025**, *6*, 20240077. https://doi.org/10.1002/VIW.20240077